NOTES AND CORRESPONDENCE

Parameterization of the Optical Properties of Sulfate Aerosols in the Infrared

J. LI

Canadian Center For Climate Modeling and Analysis, Meteorological Service of Canada, University of Victoria, Victoria, British Columbia, Canada

QILONG MIN

ASRC, The University at Albany, State University of New York, Albany, New York

25 April 2001 and 11 April 2002

ABSTRACT

Parameterizations of absorptance depth for ammonium sulfate [$(NH_4)_2SO_4$], ammonium bisulfate (NH_4HSO_4), and sulfuric acid (H_2SO_4) in the infrared are provided for an eight-band model (covering 340–2500 cm^{-1}) and for 32 individual wavenumbers in order to generate other band schemes. The parameterization is simple in form and in its dependence on relative humidity.

It is found that the aerosol surface infrared forcing can cancel about 12%–24% aerosol surface solar forcing in a clear sky condition. Also the existence of clouds could enhance the ratio of aerosol surface infrared forcing to the aerosol surface solar forcing. In contrast to the solar case, a small mode size distribution does not always produce a larger aerosol surface forcing. Also it is found that the aerosol surface forcing is dependent on the aerosol location. Very simple analysis is presented to help understand the related physics on sulfate aerosol infrared radiative forcing.

1. Introduction

In recent years, atmospheric aerosols have been considered important for climate change because their direct forcing and indirect forcing are appreciable to alter the radiative balance. Among all aerosols, sulfate aerosols have been paid most attention, since sulfate aerosols over land are mostly an anthropogenic product and since the optical properties and size distributions of sulfate aerosols could be reasonably well known.

Most of studies on atmospheric aerosol are focused on solar radiation (Chuang et al. 1994; Mitchell et al. 1995; Nemesure et al. 1995; Liousse et al. 1996; Feichter et al. 1997; Haywood et al. 1997; Reader and Boer 1998; Grant et al. 1999; Kiehl et al. 2000; and others). Atmospheric aerosols prevent some solar photons from reaching the earth's surface. The direct forcing at the surface is therefore negative. This negative forcing could partly compensate the positive forcing caused by greenhouse gases. However, in comparison with the number sulfate aerosol solar forcing studies, sulfate aerosol infrared forcing has been paid less attention.

To perform radiative transfer calculations that account for aerosol effects, the related aerosol optical properties are required. From observations, all sulfate aerosol particles grow in size as relative humidity increases (Tang and Munkelwitz 1994; Tang 1996). Therefore, like the parameterization of the aerosol optical properties for solar radiation, the parameterization for aerosol infrared optical properties is also a function of relative humidity.

To understand the mechanics for the aerosol infrared forcing, we will implement the proposed parameterization scheme in a column radiative transfer model to illustrate what the magnitude is for aerosol infrared forcing.

Li et al. (2001, hereafter Li01) proposed a parameterization of sulfate aerosol optical properties for solar radiation, which could be easily implemented within climate models. This work completes Li01 by extending the parameterization to the infrared.

2. Parameterization of absorptance coefficient

It is known that, in the troposphere, the dominant sulfate compounds are ammonium sulfate [$(NH_4)_2SO_4$], ammonium bisulfate (NH_4HSO_4), and sulfuric acid

Corresponding author address: Dr. Jiangnan Li, Canadian Center For Climate Modeling and Analysis, Meteorological Service of Canada, P. O. Box 1700, University of Victoria, Victoria, BC V8P 2Y2, Canada.
E-mail: Jiangnan.Li@ec.gc.ca

(H_2SO_4) (Twomey 1971; Nemesure et al. 1995; and others). Recent observations show that sulfate aerosols can mix with organic species. This makes the process for calculation of sulfate aerosol radiative forcing much more complicated. First, the refractive indexes for various organic species are not currently available; second, the proportions of organic species and extent of their mixing is not clear; third, as opposed to nonorganic species, organic species can change easily by chemical reaction. We must admit at the present stage we do not have the ability to properly handle the optical properties of sulfate aerosols mixing with organic species. Therefore, in the works of Kiehl et al. (2000) and others, pure sulfate aerosol without organic species mixture is assumed.

For the growth of aerosol particles, the growth factor η is defined as the ratio of the aerosol particle radius r at a specified $\mathcal{H}$ (the relative humidity normalized to unity) to the radius of the corresponding dry aerosol r_d:

$$\frac{r}{r_d} = \eta(r_d, \mathcal{H}). \tag{1}$$

In our calculations, the aerosol growth is obtained using the traditional Köhler curve with recent development in equilibrium saturation theory considered (see Li01).

The size distribution of many types of aerosol particles in the atmosphere tends to closely resemble lognormal distributions. A single-mode distribution has the following form:

$$n(r) = \frac{dN}{dr} = \frac{N_0}{\sqrt{2\pi}r\,\ln\sigma}\exp\left[-\frac{(\ln r - \ln r_0)^2}{2(\ln\sigma)^2}\right]. \tag{2}$$

A multimodal distribution is obtained by simply summing single-mode distributions. In (2), r is the radius of the aerosol particle, N_0 is the total number density, r_0 is the geometric mean radius (for the mode), and σ is the geometric standard deviation. The effective radius and effective variance for the lognormal distribution are easily obtained as $r_e = r_0 \exp[2.5(\ln\sigma)^2]$ and $v_e = \exp[(\ln\sigma)^2] - 1$.

The wet size distribution $n(r)$ is related to the dry size distribution $n(r_d)$ in the following way:

$$n(r_d) \rightarrow n(r) = n\left(\frac{r}{\eta}\right)\frac{d(r/\eta)}{dr}. \tag{3}$$

This prescription constrains the conservation of particle number in the growth process. The number of dry particles in the interval from r_d to $r_d + dr_d$ is required to equal the number of wet particles in the interval from r to $r + dr$. That is, $n(r_d)dr_d = n(r)dr$. As the particles grow, the wet size distribution $n(r)$ will shift toward larger radius size, and the wet size distribution may be distorted from the lognormal form. However, based on (3), the manner in which the wet size distribution is related to the dry size distribution, an average of a physical quantity $F(r)$ weighted by a wet size distribution can be obtained from the dry distribution:

$$\overline{F} = \int_0^\infty F(r)n(r)\,dr/N_0 = \int_0^\infty F(\eta r_d)n(r_d)\,dr_d/N_0. \tag{4}$$

In most climate models, usually only the size distribution for dry aerosol is specified. Because of growth, wet optical properties will be significantly dependent on the wet aerosol distribution, especially for high relative humidities. But with the relation shown in (4) the wet optical properties are analytically related to the dry size distribution. The exact size distribution weighted physical quantities can be obtained without explicit determination of the wet aerosol size distribution.

In the infrared the absorption effect is dominant and the absorption approximation is widely used:

$$\mu\frac{dI(\tau, \mu)}{d\tau} = (1 - \tilde{\omega})I(\tau, \mu) - (1 - \tilde{\omega})B(T), \tag{5}$$

where $\mu = \cos\theta$, θ is the zenith angle, τ is the optical depth, $\tilde{\omega}$ is the single scattering albedo, and $B(T)$ is the blackbody emission at temperature T.

If we define an absorptance depth $\kappa = \tau(1 - \omega)$ Eq. (5) is simplified as

$$\mu\frac{dI(\kappa, \mu)}{d\kappa} = I(\kappa, \mu) - B(T). \tag{6}$$

Like optical depth, we also can separate out the wet aerosol content (WAC) from the absorptance depth: $\kappa = \mathrm{WAC}\xi$, where we call ξ the specific absorptance, and

$$\xi = \psi(1 - \omega), \tag{7}$$

where ψ is the specific extinction.

Since the initial source of aerosols is considered dry, we can also write

$$\kappa = \mathrm{DAC}\mathcal{R}\xi, \tag{8}$$

where $\mathcal{R} = \mathrm{WAC/DAC}$, is the ratio of wet to dry aerosol contents. The DAC and WAC are defined by

$$\mathrm{DAC} = \frac{4\pi\rho_d}{3}\int n(r_d)r_d^3\,dr_d, \tag{9}$$

where ρ_d is the mass density of the dry aerosols, and

$$\mathrm{WAC} = \frac{4\pi}{3}\int \rho n(r_d)(\eta r_d)^3\,dr_d, \tag{10}$$

where ρ is the mass density of wet particles, a function of $\mathcal{H}$.

From (7) the specific absorptance at wavenumber λ is

$$\xi_\lambda = \frac{\pi\int[Q_{\mathrm{ext}}(\lambda, \eta r_d) - Q_{\mathrm{sca}}(\lambda, \eta r_d)](\eta r_d)^2 n(r_d)\,dr_d}{\int\frac{4\pi\rho}{3}n(r_d)(\eta r_d)^3\,dr_d}, \tag{11}$$

TABLE 1. Coefficients in (12) for the ratio of wet to dry aerosol content.

Sulfate	k_1	k_2	k_3	k_4
$(NH_4)_2SO_4$	−0.2373	1.135	0.010 48	1.06
NH_4HSO_4	−0.0611	0.7515	0.029 56	1.10
H_2SO_4	0.2515	1.147	0.008 723	1.049

where Q_{ext} is the extinction efficiency and Q_{sca} is the scattering efficiency.

For our calculations, we use the refractive indexes of water and sulfate the same as Li01.

Measurements show that the aerosol distributions usually have an effective radius in the range from 0.1 to 1 μm (Lacis and Mishchenko 1995) in a lognormal distribution. As in the parameterization for solar radiation, three effective radii are considered: 0.166, 0.5, and 1 μm. Note that these values of effective radius correspond to dry aerosol sizes. To obtain the optical properties for other values of effective radius, an appropriate interpolation technique can be employed. An effective variance of 0.693 is used in all calculations for the dry aerosol distribution (Chýlek and Wong 1995; Li01).

We find that $\mathcal{R}$ is strongly dependent on the relative humidity $\mathcal{H}$, but largely insensitive to changes in the effective radius of the dry aerosol size distribution. Also, it is found that $\mathcal{R}$ is insensitive the changes in the effective variance. Therefore, the parameterization of $\mathcal{R}$ is taken as independent of effective radius of the original dry particle distribution. Here, $\mathcal{R}$ is parameterized as

$$\mathcal{R} = \exp\left[k_1 + k_2\mathcal{H} + \frac{k_3}{(\mathcal{H} - k_4)^2}\right]. \qquad (12)$$

The coefficients for each sulfate aerosol are relisted in Table 1 (there are two errors in sign in Table 1 of Li01). For $(NH_4)_2SO_4$, the parameterization is valid for $0.35 < \mathcal{H} < 0.98$, and for below the crystallization point $\mathcal{R} = 1$. The parameterization for NH_4HSO_4 and H_2SO_4 is valid for $0.05 < \mathcal{H} < 0.98$. Given the fractional yield of emitted SO_2 gas that will react to produce sulfate aerosols and the dry loading of the sulfate aerosol, we can use $\mathcal{R}$ to obtain the wet sulfate loading.

The averaged value of specific absorptance for band i is defined as

$$\xi_i = \int_{\Delta\lambda_i} \xi_\lambda B_\lambda(T)\, d\lambda \Big/ \int_{\Delta\lambda_i} B_\lambda(T)\, d\lambda, \qquad (13)$$

where $B_\lambda(T)$ is the Planck function, T is the temperature, and $\Delta\lambda_i$ is the spectral interval for band i. Equation (13) is physically similar to the Chandraskhar mean (Liou 1992).

We consider an eight-band scheme covering 340–2500 cm^{-1}. In the range of 0–340 cm^{-1}, the refractive index for sulfate aerosol is not currently available. Also, the fractional weight of the Planck function in this range is very small. The specific absorptance for each band (i) is parameterized in the following way:

$$\xi_i = a_1^i + a_2^i\mathcal{H} + \frac{a_3^i}{(\mathcal{H} - 1.05)}. \qquad (14)$$

The parameterization coefficients a_1^i, a_2^i, and a_3^i are provided in Table 2 for sulfuric acid, ammonium sulfate, and ammonium bisulfate. The last term accounts for the very rapid change in specific absorptance when $\mathcal{H}$ is close to 1.

In Fig. 1, the specific absorption for the eight-band scheme of sulfuric acid is shown with the effective radii of 0.166, 0.5, and 1.0 μm, respectively. These results show that the parameterizations of (14) are able to provide accurate values for the sulfate aerosol specific absorptance.

In Fig. 1, opposite to the solar case shown in Li01, in which the specific extinction shows completely different behavior in response to changes in $\mathcal{H}$ for different effective radius sizes, the behavior of specific absorptance in response to changes in $\mathcal{H}$ is relatively very similar for different effective radius sizes. For the solar wavelength range, the ratio of the wavelength to particle size is small; while for the infrared, the ratio becomes very large. By Mie theory the absorption is sensitive to the wavelength to particle size ratio only when the ratio is small.

For different bands, the behaviors in response to changes in $\mathcal{H}$ are very different. For bands 1 to 5, the specific absorptance decreases with the increase of $\mathcal{H}$; while for bands 7 and 8 the specific absorptance increases with the increase of $\mathcal{H}$. Though the specific absorptance depends on the specific extinction and single scattering albedo, the increase or decrease of specific absorptance is mostly determined by the behavior of specific extinction. This is because the single scattering albedo is relatively insensitive to $\mathcal{H}$.

The absorptance depth is a product of WAC and the specific absorptance. By comparing the behavior of WAC (Fig. 2 in Li01) and the behavior of specific absorptance with the change of $\mathcal{H}$, we find that the change in WAC is much larger than the change in specific absorptance as $\mathcal{H}$ increases. This means that the absorptance depth will always tend to increase, regardless of any decrease in specific absorptance.

Table 2 illustrates the specific results for the eight-band scheme. However, in order to produce other band schemes, we also present results for each single wavenumber. We use the same parameterization scheme as (14) for each single wavenumber:

$$\xi_\lambda = a_1^\lambda + a_2^\lambda\mathcal{H} + \frac{a_3^\lambda}{(\mathcal{H} - 1.05)}, \qquad (15)$$

where λ represents the wavenumber. Any band scheme can be obtained through the sum of the results for individual wavelengths with respect to the Planck function, as in (15).

TABLE 2. Coefficients in Eq. (14) for H_2SO_4, $(NH_4)_2)SO_44$, and NH_4HSO_4 for eight-band scheme; α_1, α_2, and α_3 units: $m^2\ g^{-1}$.

r_e (μm)	Band	Wavenumber (cm^{-1})	H_2SO_4			$(NH_4)_2SO_4$			NH_4HSO_4		
			α_1	α_2	α_3	α_1	α_2	α_3	α_1	α_2	α_3
0.166	1	2200–2500	1.56E−1	−1.07E−1	3.07E−4	1.20E−2	8.16E−3	−5.83E−4	1.27E−2	7.23E−3	−6.78E−4
	2	1900–2200	1.83E−1	−1.17E−1	1.88E−3	3.04E−1	−1.62E−1	6.23E−3	2.81E−1	−1.30E−1	7.85E−3
	3	1400–1900	1.90E−1	−5.69E−2	1.97E−3	3.15E−1	−1.35E−1	5.29E−3	2.90E−1	−1.01E−1	6.79E−3
	4	1100–1100	3.23E−1	−1.74E−1	5.41E−3	3.54E−1	−2.11E−1	5.25E−3	2.49E−1	−7.66E−2	8.41E−3
	5	980–1100	2.61E−1	−9.64E−2	6.44E−3	2.34E−1	4.69E−2	1.34E−2	4.28E−1	−1.10E−1	1.86E−2
	6	800–980	1.46E−1	−1.48E−3	7.51E−4	−2.35E−3	3.21E−2	−1.34E−3	9.75E−3	7.94E−2	−4.24E−3
	7	540–800	1.19E−1	8.23E−2	−4.77E−3	3.03E−2	1.37E−1	−6.75E−3	3.67E−2	1.40E−1	−7.07E−3
	8	340–540	8.57E−2	4.01E−2	−4.14E−3	−5.75E−3	1.01E−1	−3.85E−3	4.29E−3	9.14E−2	−4.38E−3
0.5	1		1.77E−1	−1.11E−1	9.33E−4	1.68E−2	1.04E−2	−6.24E−4	1.71E−2	9.64E−3	−7.43E−4
	2		1.98E−1	−1.14E−1	2.60E−3	2.74E−1	−1.23E−1	6.16E−3	2.58E−1	−1.01E−1	7.47E−3
	3		2.04E−1	−5.35E−2	2.80E−3	2.94E−1	−1.05E−1	5.20E−3	2.80E−1	−8.83E−2	6.49E−3
	4		3.23E−1	−1.62E−1	5.78E−3	3.22E−1	−1.78E−1	4.83E−3	2.54E−1	−8.33E−2	7.60E−3
	5		2.80E−1	−1.07E−1	6.77E−3	3.03E−1	−1.35E−2	1.37E−2	4.27E−1	−1.33E−1	1.63E−2
	6		1.63E−1	−7.89E−3	1.96E−3	−1.36E−3	3.60E−2	−9.26E−4	1.16E−2	8.74E−2	−3.11E−3
	7		1.30E−1	9.08E−2	−1.94E−3	2.63E−2	1.62E−1	−4.78E−3	3.79E−2	1.55E−1	−4.99E−3
	8		9.16E−2	4.74E−2	−3.75E−3	−7.97E−3	1.08E−1	−4.22E−3	2.66E−3	9.82E−2	−4.75E−3
1.0	1		1.77E−1	−1.02E−1	1.66E−3	2.22E−2	1.09E−2	−3.54E−4	2.19E−2	1.05E−2	−4.55E−4
	2		1.92E−1	−1.00E−1	3.25E−3	2.05E−1	−6.27E−2	5.43E−3	1.97E−1	−5.13E−2	6.40E−3
	3		1.98E−1	−4.71E−2	3.70E−3	2.32E−1	−5.06E−2	5.07E−3	2.32E−1	−4.37E−2	6.22E−3
	4		2.88E−1	−1.28E−1	5.92E−3	2.56E−1	−1.17E−1	4.45E−3	2.27E−1	−6.95E−2	6.48E−3
	5		2.73E−1	−1.05E−1	6.64E−3	3.25E−1	−6.14E−2	1.21E−2	3.59E−1	−1.12E−1	1.27E−2
	6		1.74E−1	−2.11E−2	3.10E−3	3.30E−3	3.59E−2	−2.26E−4	1.75E−2	9.02E−2	−1.18E−3
	7		1.42E−1	8.13E−2	1.91E−3	3.06E−2	1.75E−1	−7.06E−4	4.30E−2	1.62E−1	−8.61E−4
	8		1.03E−1	5.35E−2	−1.19E−3	−8.59E−3	1.24E−1	−2.95E−3	3.51E−3	1.10E−1	−3.49E−3

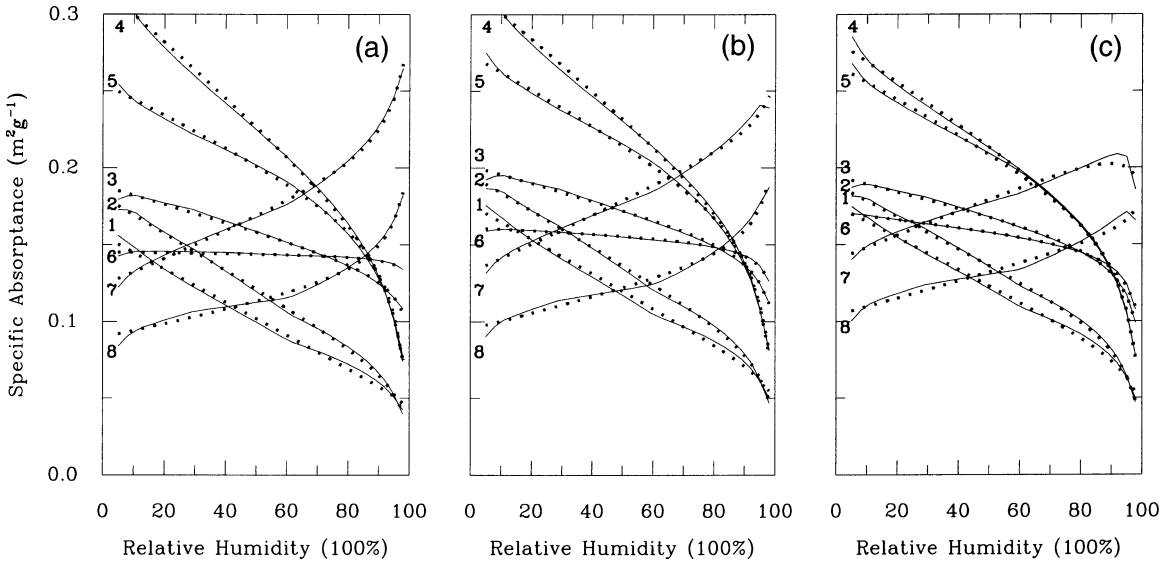

FIG. 1. The variation of the specific absorptance as functions of relative humidity for H_2SO_4. The theoretical calculations are shown as solid lines, and the parameterization results are dotted lines. The effective radius equals (a) 0.166, (b) 0.5, and (c) 1.0 μm. The numbers shown on the left sides are the band numbers.

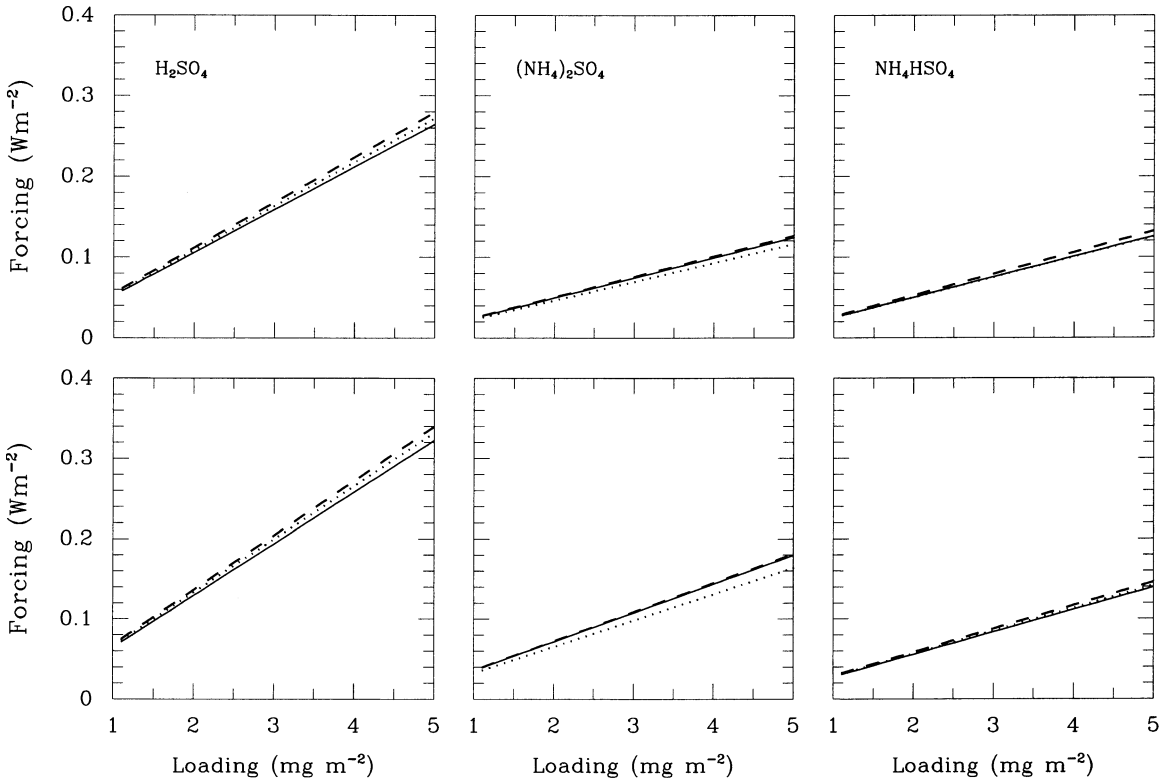

FIG. 2. Aerosol surface infrared forcing via aerosol loading: (a) H_2SO_4, (b) $(NH_4)_2SO_4$, and (c) NH_4HSO_4. The aerosols are homogeneously distributed within 2 km above the surface. The solid, dashed, and dotted lines are the results for effective radius of 0.166, 0.5, and 1 μm, respectively. The upper panels are the MLS results and the lower panels are the SAW results.

TABLE 3. Coefficients in Eq. (15) for H_2SO_4, $(NH_4)_2SO_4$, and NH_4HSO_4 with $r_e = 0.5$ μm; α_1, α_2, and α_3 units: m^2g^{-1}.

Wavenumber (cm^{-1})	H_2SO_4			$(NH_4)_2SO_4$			NH_4HSO_4		
	α_1	α_2	α_3	α_1	α_2	α_3	α_1	α_2	α_3
2500	1.92E−1	−1.6E−1	6.66E−4	3.07E−2	−0.24E−3	1.27E−4	2.89E−2	−0.54E−3	1.45E−4
2240	1.77E−1	−1.5E−1	1.21E−3	9.52E−3	0.20E−2	−1.12E−3	1.10E−2	0.97E−2	−1.33E−3
2020	1.79E−1	−1.2E−1	1.66E−3	7.06E−3	0.79E−2	−9.67E−4	8.36E−3	0.61E−2	−1.13E−3
1820	2.42E−1	−1.1E−1	3.83E−3	8.64E−3	0.29E−2	−7.27E−4	9.59E−3	0.18E−2	−8.39E−4
1680	2.50E−1	−4.8E−2	2.24E−3	−6.00E−3	0.56E−1	−3.59E−3	7.01E−3	0.40E−1	−4.40E−3
1540	1.61E−1	−3.4E−2	2.46E−3	4.93E−2	0.72E−2	−1.30E−3	4.92E−2	0.90E−2	−1.38E−3
1450	1.72E−1	−5.2E−2	2.62E−3	3.97E−1	−0.14E−1	6.35E−3	3.48E−1	−0.44E−1	8.84E−3
1390	1.92E−1	−7.9E−2	3.29E−3	4.09E−1	−0.56E−1	1.13E−2	4.36E−1	−0.92E−1	1.21E−2
1270	2.85E−1	−1.8E−1	2.74E−3	5.90E−2	−0.81E−4	−2.81E−4	5.76E−2	0.52E−3	−2.77E−4
1250	3.40E−1	−2.4E−1	3.86E−3	6.76E−2	−0.52E−3	−9.58E−5	6.41E−2	−0.71E−3	−1.69E−5
1210	4.57E−1	−2.3E−1	9.90E−3	1.03E−1	−0.23E−2	6.53E−4	9.35E−2	−0.93E−2	9.88E−4
1170	4.28E−1	−2.1E−1	9.36E−3	2.46E−1	−0.28E−1	3.49E−3	2.11E−1	−0.05E−2	4.82E−3
1150	3.83E−1	−2.5E−1	6.83E−3	5.41E−1	−0.36E−1	8.47E−3	4.32E−1	−0.93E−1	1.22E−2
1110	2.90E−1	−1.6E−1	7.09E−3	1.31E+0	−0.92E−1	2.05E−2	8.58E−1	−0.59E−1	3.82E−2
1080	2.87E−1	−1.1E−1	5.67E−3	7.05E−1	−0.71E−2	3.48E−2	8.64E−1	−0.73E−1	4.54E−2
1050	3.66E−1	−1.8E−1	9.77E−3	2.50E−1	−0.59E−2	9.72E−3	3.65E−1	−0.57E−1	1.00E−2
1020	2.57E−1	−8.4E−2	6.83E−3	1.13E−1	−0.14E−3	2.50E−3	1.45E−1	−0.18E−2	2.69E−3
990	1.89E−1	−3.9E−2	5.54E−3	6.41E−2	0.12E−2	5.09E−4	8.01E−2	−0.20E−3	5.65E−4
950	1.44E−1	−6.6E−3	3.71E−3	2.01E−2	0.12E−2	−1.18E−3	3.01E−2	0.05E−2	−1.32E−3
910	2.00E−1	−5.4E−2	2.67E−3	7.78E−3	0.75E−2	−1.95E−3	1.96E−2	0.47E−2	−2.22E−3
870	1.77E−1	−1.1E−2	1.15E−3	−7.77E−3	0.05E−1	−2.84E−3	7.39E−3	0.87E−2	−3.28E−3
840	1.30E−1	3.3E−2	−6.39E−4	−1.59E−2	0.30E−1	−3.41E−3	1.73E−3	0.11E−1	−3.96E−3
800	1.09E−1	9.3E−2	−7.78E−4	−2.58E−2	0.84E−1	−4.19E−3	−2.06E−3	0.57E−1	−4.94E−3
760	1.09E−1	1.1E−1	−8.07E−4	−2.98E−2	0.06E−1	−4.65E−3	−3.90E−3	0.77E−1	−5.51E−3
700	1.15E−1	1.9E−1	−1.05E−3	−3.23E−2	0.26E−1	−5.30E−3	−5.94E−3	0.95E−1	−6.32E−3
670	1.22E−1	1.0E−1	−1.32E−3	−2.62E−2	0.20E−1	−5.36E−3	−3.95E−3	0.91E−1	−6.60E−3
600	1.89E−1	3.6E−2	−2.42E−3	5.60E−2	0.61E−1	−3.56E−3	1.93E−1	0.32E−2	−8.35E−4
580	1.69E−1	3.2E−2	−3.35E−3	−2.63E−2	0.77E−1	−6.71E−3	7.70E−3	0.60E−1	−6.30E−3
550	1.15E−1	6.3E−2	−3.85E−3	−2.60E−2	0.71E−1	−6.09E−3	−3.18E−3	0.54E−1	−6.43E−3
500	9.74E−2	5.2E−2	−3.59E−3	−1.83E−2	0.36E−1	−5.17E−3	−3.14E−3	0.23E−1	−5.68E−3
440	8.89E−2	2.5E−2	−3.97E−3	−9.75E−3	0.08E−1	−4.27E−3	9.82E−4	0.79E−2	−4.80E−3
400	6.41E−2	3.7E−2	−3.97E−3	−2.25E−3	0.81E−2	−3.54E−3	5.51E−3	0.98E−2	−4.06E−3

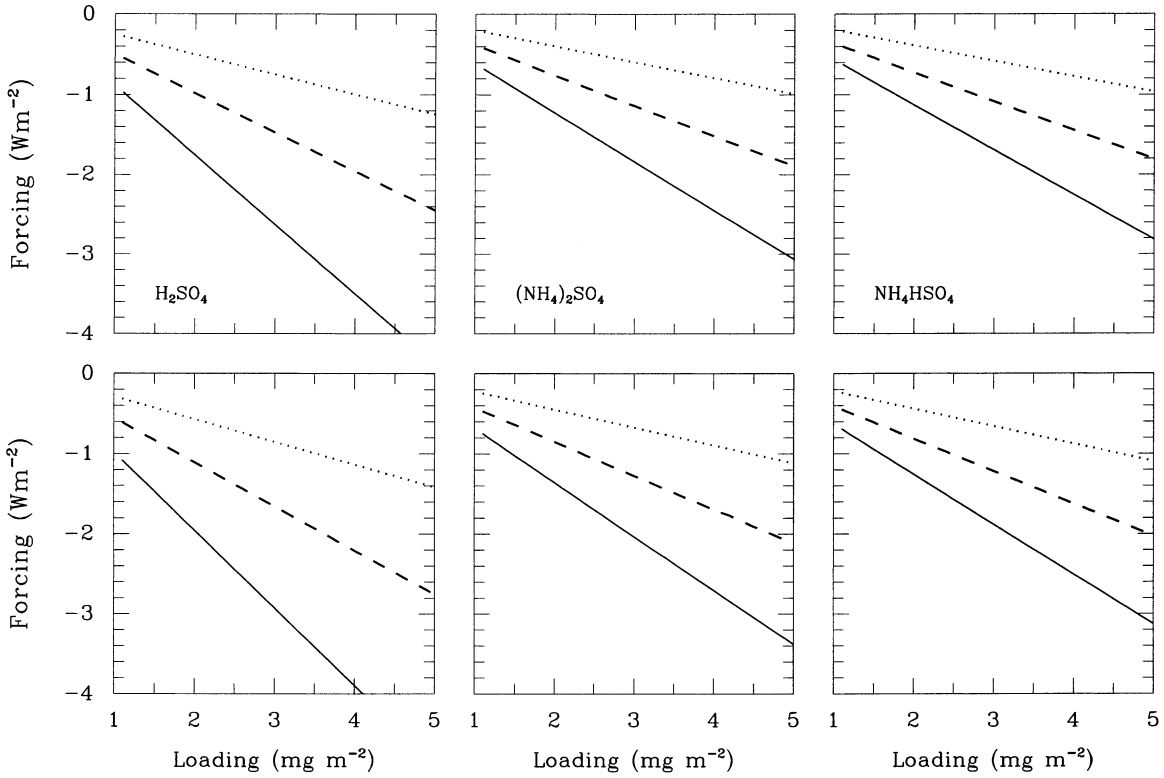

FIG. 3. The same as Fig. 2 but for sulfate aerosol surface solar forcing. The solar zenith angle is 50.6°. The solid, dashed, and dotted lines are the results for effective radius of 0.166, 0.5, and 1 μm, respectively.

The results of the specific absorptance for 32 individual wavenumbers are listed in Table 3 covering the range of 400–2500 cm^{-1}. The distribution of the chosen wavenumber is not even. We consider more cases near the window region, since higher radiative energy is weighted for the window region at the atmospheric temperature conditions. Since the specific absorptance is not sensitive to the effective radius, only the results of $r_e = 0.5$ μm are presented.

3. Sulfate aerosol surface infrared radiative forcing

For the upward flux in the infrared, the aerosols act like greenhouse gases to prevent radiation loss directly to space. However, this effect is very small (see later discussion). Aerosols can reduce the downward flux and also can enhance the emission to the surface. The aerosol direct forcing for the downward flux is determined by these two opposing factors.

We investigated the aerosol infrared forcing using a one-dimensional radiative transfer model instead of using general circulation models (GCMs), since it is much easier for us to understand the crucial factors determining aerosol infrared direct forcing.

We used the radiation model for CCC GCM in the Canadian Center for Climate Modeling and Analysis model, which is a model using a correlated-*k* distribution for gaseous transmission. The continuum scheme is based on numerical calculations from LBLRTM (Mlawer et al. 1997). For cloud and aerosol optical properties, there are nine bands for the infrared, covering from 0–2500 cm^{-1}.

Usually it is believed that aerosols are well mixed within boundary layer (usually 1 $\sim$ 2 km) due to turbulence. Above the boundary layer, the aerosol concentration decays exponentially. In Fig. 2 the surface forcing via aerosol loading is shown. For simplicity, aerosol is assumed to be homogeneously loaded within 2 km above the surface. Two atmospheric profiles of middle latitude summer (MLS; upper panels) and subarctic winter (SAW; lower panels) are considered. The global averaged loading of SO_4^{--} is about 2 mg m^{-2} (Feichter et al. 1995; Kiehl et al. 2000). If the sulfate aerosol is specified to be H_2SO_4, the loading will exhibit almost no change, since the molecular weights for SO_4^{--} and H_2SO_4 are close. If the sulfate aerosol is specified to be $(NH_4)_2SO_4$, the loading will increase about 30%. And if the sulfate aerosol is specified to be NH_4HSO_4, the loading will increase about 15%.

For a sulfate aerosol loading of 2.5 mg m^{-2}, the surface forcing is about 0.06 $\sim$ 0.1 W m^{-2} for $(NH_4)_2SO_4$. The forcing for H_2SO_4 is higher. We present the corresponding surface solar forcing in Fig. 3 with the solar zenith angle set to the diurnal mean of 50.6°. We find that unlike aerosol surface infrared forcing, the aerosol

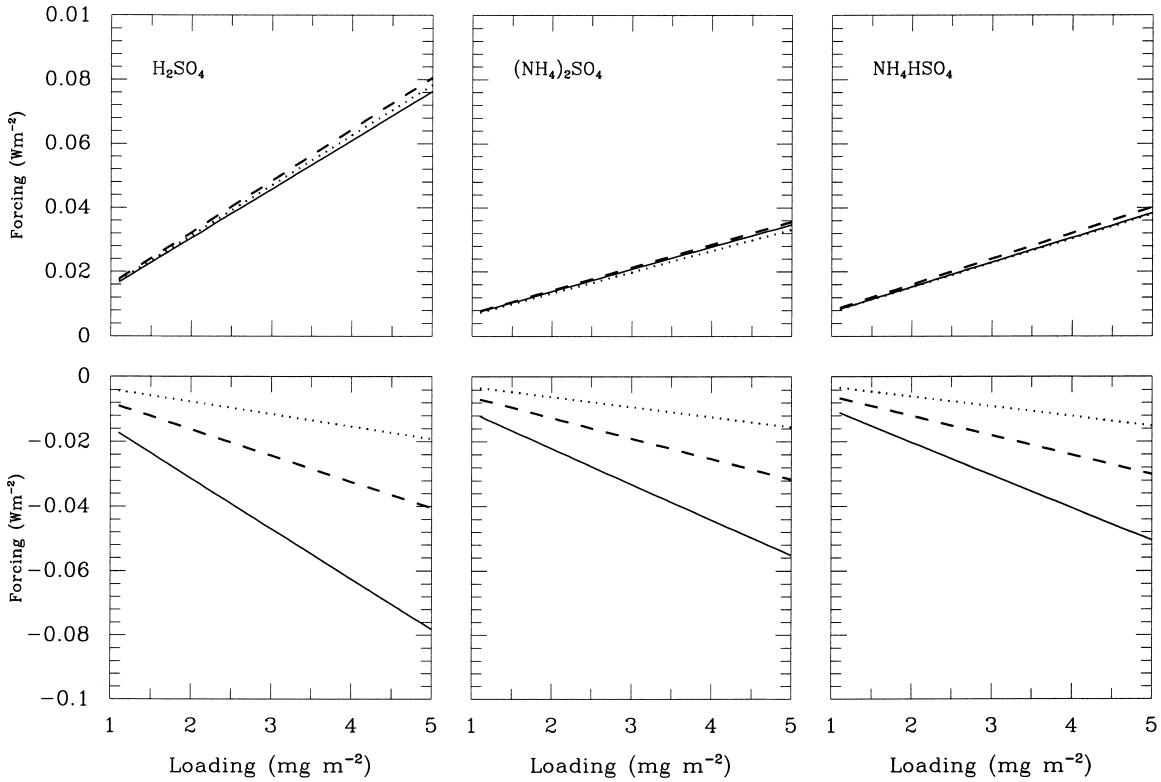

FIG. 4. An MLS atmospheric profile of a cloud located between 4 and 5 km. (top) The aerosol surface infrared forcing via aerosol loading with aerosol condition the same as Fig. 2; (bottom) the aerosol surface solar forcing via aerosol loading with aerosol condition the same as Fig. 3.

surface solar forcing is very sensitive to the aerosol size. Aerosols with a small effective radius can produce a much larger forcing than aerosols with a larger effective radius.

Comparing Fig. 2 and Fig. 3, we see the surface infrared forcing could be about 6% $\sim$ 10% of the surface solar forcing for $(NH_4)_2SO_4$, and the surface infrared forcing could be about 12% of the surface solar forcing for H_2SO_4. These are relatively small. However, the aerosol solar forcing only exists in the daytime, but the aerosol infrared forcing exists all day. As a result, the aerosol infrared forcing has to be doubled when comparing it with the aerosol solar forcing. Therefore, the aerosol surface infrared forcing can actually cancel about 12%–24% surface solar forcing.

The aerosol infrared surface forcing for tropical profile is not shown in Fig. 2. By using a tropical sounding the results are similar to MLS except about 10% lower in magnitude.

As mentioned before, the shade of cloud over aerosols will reduce the aerosol surface solar forcing, since the downward solar flux could be dramatically reduced, thus the difference in flux caused by existing aerosols will also be reduced. However, the influence of cloud to aerosol surface infrared forcing could be smaller than that of solar, since the downward infrared flux contributed from the emission below the cloud will not change. Figure 4 shows the aerosol surface forcing change with a cloud located between 4 and 5 km. The aerosol conditions are the same as those in Figs. 2 and 3. In comparison with Figs. 2 and 3, the surface infrared forcing is about 30% of the results without clouds, while the surface solar forcing is only about 2% of the results without clouds. Therefore, the existence of cloud could enhance the ratio of aerosol surface infrared forcing to the aerosol surface solar forcing.

In the following we present the simple analytical solution of (6), which can help us to understand the physics related to the aerosol infrared forcing. We assume that level 1 is the top of the atmosphere, level N is the surface, and layer i is between level i and level $i + 1$. For simplicity, we use isothermal source, that is, constant Planck function B_i determined by the temperature at the middle of the layer i. The solution for ith layer is

$$F_i^+ = F_{i+1}^+ e^{-\kappa_i/\mu_1} + (1 - e^{-\kappa_i/\mu_1})\tilde{B}_i, \qquad (16a)$$

$$F_{i+1}^- = F_i^- e^{-\kappa_i/\mu_1} + (1 - e^{-\kappa_i/\mu_1})\tilde{B}_i, \qquad (16b)$$

where F_i^+ (F_i^-) is the upward (downward) flux at level i, $1/\mu_1 = e^{1/2} = 1.648\ 721\ 3$ (Li 2000) is the diffusivity factor, and $\tilde{B}_i = \pi B_i$. Note that in the column radiative transfer model we use a nonisothermal source function. The isothermal source of a constant Planck function

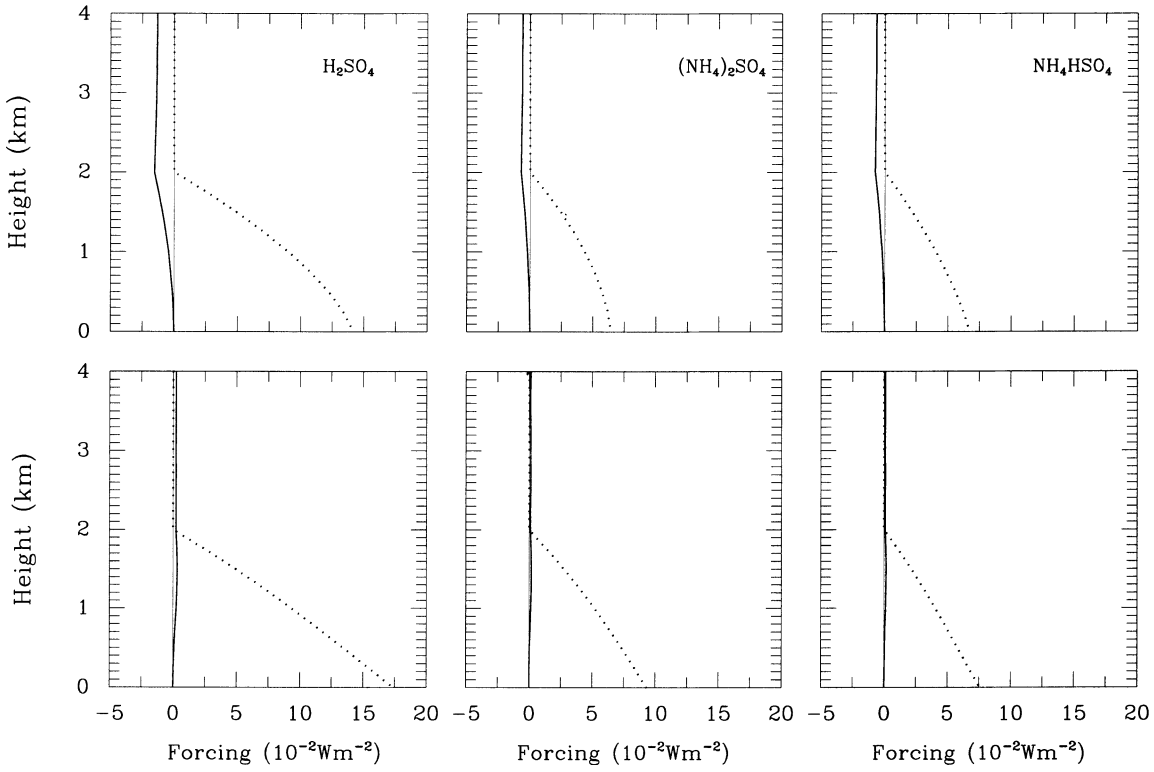

FIG. 5. Aerosol infrared forcing profiles. The solid (dotted) lines are the differences in the upward (downward) flux caused by the existence of aerosol. The loading is 2.5 mg m^{-2}. The effective radius is 0.5 μm. The aerosol is distributed homogeneously between 0 and 2 km. (top) The MLS results and (bottom) the SAW results.

presented here is only for the purposes of illustrating the related physics for aerosol forcing.

Since the aerosol absorptance depth is very small, the forcing can be considered as a perturbation result. Therefore, if aerosol absorptance depth for the ith layer is $\Delta\kappa_i$, the changes in upward flux at level i and downward flux at level $i + 1$ are

$$\Delta F_i^+ = -(F_{i+1}^+ - \tilde{B}_i)e^{-\kappa_i/\mu_1}\Delta\kappa_i, \quad (17a)$$

$$\Delta F_{i+1}^- = -(F_i^- - \tilde{B}_i)e^{-\kappa_i/\mu_1}\Delta\kappa_i. \quad (17b)$$

Figure 2 shows that the aerosol surface infrared forcing is always linearly proportional to the aerosol loading, which supports the perturbation theory. The downward flux is very small at the high altitude and it gradually increases with a decrease in height. Therefore, generally, $F_i^- - \tilde{B}_i < 0$ and ΔF_{i+1}^- is positive. For the upward flux, if the temperature decreases with height in the lower atmosphere, the upward flux would also decrease with height in the lower atmosphere, thus $F_{i+1}^+ - \tilde{B}_i > 0$ and the forcing is negative. However, if temperature inver-

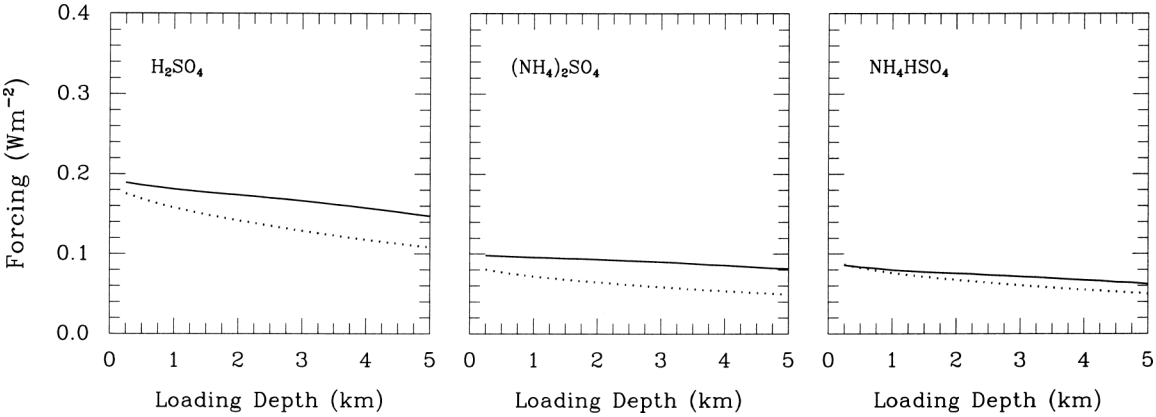

FIG. 6. Aerosol surface infrared forcing via aerosol vertical stretch in the distribution. The loading is 2.5 mg m^{-2}. The effective radius is 0.5 μm. The aerosol is distributed homogeneously. The solid lines are MLS results, and the dotted lines are SAW results.

sion occurs in the lower atmosphere, the incoming flux F^+_{i+1} may be smaller than the layer emission $\tilde{B}_i$ and forcing could be positive.

In Fig. 5 the changes of upward and downward flux due to the existence of aerosols are shown. The cases are the same as Fig. 2 with aerosol loading 2.5 mg m^{-2}. We find that the model results are consistent with the above analysis. Since the temperature profile is slightly inverted below 2 km in SAW, the forcing for the upward flux is slightly positive.

It is found from Fig. 5 (clearly shown in the data) that above the aerosol existing layer, the forcing of upward flux always deceases with height. If aerosol in i layer produce forcing ΔF^+_i at level i, the flux at level $i - 1$ is

$$F^+_{i-1} = (F^+_i - \tilde{B}_{i-1})e^{-\kappa_{i-1}/\mu_1} + \tilde{B}_{i-1} + \Delta F^+_i e^{-\kappa_{i-1}/\mu_1}. \quad (18)$$

Therefore, the forcing of upward flux at level $i - 1$ becomes $\Delta F^+_i e^{-\kappa_{i-1}/\mu_1}$ with an attenuation factor. This process continues to level 1, and the forcing becomes $\Delta F^+_i e^{-(\kappa_{i-1}+\kappa_{i-2}+\cdots+\kappa_1)/\mu_1}$. We therefore can draw an interesting conclusion from the above discussion: in the infrared, the further one goes away from the perturbation region, the less perturbation can be observed. In other words, to some extent the infrared flux has the ability to adjust itself from the perturbations in the transfer process.

The aerosol surface infrared forcing is also determined by the location of the aerosol. In Fig. 6, the aerosol loading is set to a constant 2.5 mg m^{-2}, but the vertical stretch of the distribution varies from 0.25 to 5 km. The effective radius is 0.5 μm for all types of sulfate aerosol. It was found that for the same amount of aerosol loading, the surface forcing is larger when the aerosol is more concentrated near the surface. However, we must ask whether this is generally true and what are the relevant physics for this.

If the aerosol is loaded in the first layer above the surface, we only need to consider the radiative transfer process in layer $N - 1$:

$$F^-_N = F^-_{N-1}e^{-\kappa_{N-1}/\mu_1} + \tilde{B}_{N-1}(1 - e^{-\kappa_{N-1}/\mu_1}). \quad (19)$$

Therefore, the aerosol surface forcing is

$$\Delta F^{(1)} = -\frac{1}{\mu_1}(F^-_{N-1} - \tilde{B}_{N-1})e^{-\kappa_{N-1}/\mu_1}\Delta\kappa_{N-1}, \quad (20)$$

where $\Delta\kappa_i$ is the perturbation of absorptance depth by aerosol for layer i.

If the aerosol is loaded in the first two layers above the surface, the change in the downward flux at level $N - 1$ is

$$\Delta F^-_{N-2} = -\frac{1}{\mu_1}(F^-_{N-2} - \tilde{B}_{N-2})e^{-\kappa_{N-2}/\mu_1}\Delta\kappa_{N-2}, \quad (21)$$

and the surface forcing is

$$\Delta F^{(2)} = -\frac{1}{\mu_1}(F^-_{N-1} - \tilde{B}_{N-1} - \Delta F^-_{N-2})e^{-\kappa_{N-1}/\mu_1}\Delta\kappa_{N-1}. \quad (22)$$

Since the total loading for the two cases is the same, $\Delta\kappa_{N-1}$ ($=\Delta\kappa_{N-2}$) in (22) is equal to $0.5\Delta\kappa_{N-1}$ in (20), we denote it as $0.5\Delta\kappa$. Thus,

$$\Delta F^{(1)} - \Delta F^{(2)} = -0.5\frac{1}{\mu_1}(F^-_{N-1} - \tilde{B}_{N-1})e^{-\kappa_{N-1}/\mu_1}\Delta\kappa + \frac{1}{\mu_1^2}(F^-_{N-2} - \tilde{B}_{N-2})e^{-(\kappa_{N-1}+\kappa_{N-2})/\mu_1}(\Delta\kappa)^2. \quad (23)$$

Since $\Delta\kappa$ is very small, the first term dominates. As we mentioned, generally, $F^-_i - \tilde{B}_i < 0$. Therefore, $\Delta F^{(1)} - \Delta F^{(2)}$ is positive. The results of (23) hold true for the multilayer case. Therefore, the aerosol surface forcing is larger for the case with more aerosols located near the surface. Of course, in the particular case with very strong temperature inversion, which leads $F^-_i - \tilde{B}_i > 0$, the results could be opposite.

In summary, a simple parameterization of the sulfate aerosol infrared optical properties as a function of relative humidity is presented in this note. It is found that sulfate aerosol absorptance is sensitive to relative humidity but not sensitive to particle size distribution. It is found that the aerosol surface infrared forcing can cancel about 12%–24% aerosol surface solar forcing in clear sky conditions. Also in this note the mechanics for aerosol infrared forcing is discussed.

Acknowledgments. We are grateful to Drs. J. Fyfe and L. Harrison, and two anonymous reviewers for their helpful comments. Part of this research was supported by the Office of Science, Biological and Environmental Research Program (BER), U.S. Department of Energy, through the Northeast Regional Center of the National Institute for Global Environmental Change (NIGEC) under Cooperative Agreement No. DE-FC03-90ER61010.

REFERENCES

Chuang, C. C., J. E. Penner, K. E. Taylor, and J. J. Walton, 1994: Climate effects of anthropogenic sulfate: Simulations from a coupled chemistry/climate model. Preprints, *Conf. on Atmospheric Chemistry*, Nashville, TN, Amer. Meteor. Soc., 170–174.

Chýlek, J., and J. G. D. Wong, 1995: Effect of absorbing aerosols on global radiation budget. *Geophys. Res. Lett.,* **22,** 929–931.

Feichter, J., U. Lohmann, and I. Schult, 1997: The atmospheric sulfur cycle in ECHAM-4 and its impact on shortwave radiation. *Climate Dyn.,* **13,** 235–246.

Grant, K. E., C. C. Chuang, A. S. Grossman, and J. E. Penner, 1999: Modeling the spectral optical properties of ammonium sulfate and biomass burning aerosols: Parameterization of relative humidity effects and model results. *Atmos. Environ.,* **33,** 2603–2620.

Haywood, J. M., V. Ramaswamy, and L. J. Donner, 1997: A limited-area-model case study of the effects of sub-grid scale variations in relative humidity and cloud upon the direct radiative forcing of sulfate aerosol. *Geophys. Res. Lett.,* **24,** 143–146.

Kiehl, J. T., T. L. Schneider, P. J. Rasch, M. C. Barth, and J. Wong, 2000: Radiative forcing due to sulfate aerosols from simulations with the National Center for Atmospheric Research community climate model, version 3. *J. Geophys. Res.*, **105,** 1441–1457.

Lacis, A. A., and M. I. Mishchenko, 1995: Climate forcing, climate sensitivity, and climate response: A radiative modeling perspective on atmospheric aerosols. *Aerosol Forcing of Climate*, R. J. Charlson and J. Heintzenberg, Eds., John Wiley and Son, 11–42.

Li, J., 2000: Gaussian quadrature and its application to infrared radiation. *J. Atmos. Sci.*, **57,** 753–765.

——, J. G. D. Wong, J. S. Dobbie, and P. Chylek, 2001: Parameterization of the optical properties and growth of sulfate aerosols. *J. Atmos. Sci.*, **58,** 193–209.

Liou, K.-N., 1992: *Radiative Transfer and Cloud Process in the Atmosphere*. Oxford University Press, 478 pp.

Liousse, C., J. E. Penner, C. Chuang, J. J. Walton, H. Eddleman, and H. Cachier, 1996: A global three-dimensional model study of carbonaceous aerosols. *J. Geophys. Res.*, **101,** 19 411–19 432.

Mitchell, J. F. B., T. C. Johns, J. M. Gregory, and S. F. B. Tebb, 1995: Climate response to increasing levels of greenhouse gases and sulfate aerosols. *Nature*, **367,** 501–504.

Mlawer, E. J., S. J. Taubman, P. D. Brown, M. J. Iacono, and S. A. Clough, 1997: Radiative transfer for inhomogeneous atmosphere: RRTM, a validated correlated-*k* model for the longwave. *J. Geophys. Res.*, **102,** 16 663–16 682.

Nemesure, S., R. Wagener, and S. E. Schwartz, 1995: Direct shortwave forcing of climate by the anthropogenic sulfate aerosol—Sensitivity to particle size, composition, and relative humidity. *J. Geophys. Res.*, **100,** 26 105–26 116.

Reader, M. C., and G. J. Boer, 1998: The modification of greenhouse gas warming by the direct effect of sulfate aerosols. *Climate Dyn.*, **14,** 593–607.

Tang, I. N., 1996: Chemical and size effects of hygroscopic aerosols on light scattering coefficients. *J. Geophys. Res.*, **101,** 19 245–19 250.

——, and H. R. Munkelwitz, 1994: Water activities, densities, and refractive indices of aqueous sulfates and sodium nitrate droplets of atmospheric importance. *J. Geophys. Res.*, **99,** 18 801–18 808.

Twomey, S., 1971: The composition of cloud nuclei. *J. Atmos. Sci.*, **28,** 377–381.